Multielement spectrometer for efficient measurement of the momentum transfer dependence of inelastic x-ray scattering

T. T. Fister and G. T. Seidler[a)]
Physics Department, University of Washington, Seattle, Washington 98195

L. Wharton
Physics Department, University of California, Davis, California 95616

A. R. Battle and T. B. Ellis
Physics Department, University of Washington, Seattle, Washington 98195

J. O. Cross and A. T. Macrander
Advanced Photon Source, Argonne National Lab, Argonne, Illinois 60439

W. T. Elam
Applied Physics Laboratories, University of Washington, Seattle, Washington 98195

T. A. Tyson
Department of Physics, New Jersey Institute of Technology, Newark, New Jersey 07102

Q. Qian
NJ-XRSTECH Company, Bloomfield, New Jersey 07003

Nonresonant x-ray Raman scattering (XRS) is the inelastic scattering of hard x rays from the K shell of low-Z elements or the less tightly bound shells of heavier elements. In the limit of low momentum transfer q, XRS is determined by the same transition matrix element as is measured by x-ray absorption spectroscopies. However, XRS at higher q can often access higher order multipole transitions which help separate the symmetry of various contributions to the local density of states. The main drawback of XRS is its low cross section—a problem that is compounded for a q-dependent study. To address this issue, we have constructed a multielement spectrometer to simultaneously measure XRS at ten different values of q. By means of example, we report new measurements of the XRS from the L- and K-edges of Mg. This instrument is now available to general users at the Advanced Photon Source as the lower energy resolution inelastic x-ray scattering (LERIX) spectrometer. © 2006 American Institute of Physics. [DOI: 10.1063/1.2204581]

I. INTRODUCTION

Inelastic x-ray scattering (IXS) has a rich history and has an important role in many parts of contemporary research in molecular and condensed phases of matter.[1–9] Multiple beam lines at x-ray synchrotrons worldwide are now dedicated to the measurement of various different types of IXS, with each instrument reflecting the interests of its developers and users through different energy resolutions, momentum transfers, monochromator bandwidths, and scanning modes for energy loss.[4,8,10–14]

One type of IXS measurement which is poised to play a growing role in structural and electronic studies is the inelastic scattering from the core shells of low-Z elements or the less tightly bound shells of heavier elements; this IXS is often called nonresonant x-ray Raman scattering (XRS). While a critical, early XRS experiment was performed in the laboratory,[15] it is only with the advent of the second- and especially third-generation synchrotron x-ray sources that XRS measurements can be performed for a wide range of materials. This has led to a steady increase in the applica-

tions of XRS (Refs. 12 and 16–39) and in the development of instrumentation optimized for XRS measurements. To date, several XRS spectrometers have been built which use multiple spherically bent analyzers to increase the collection angle for the IXS, resulting in faster measurements.[4,12,13] However, these instruments generally operate only in the limit of low momentum transfer q, integrate over q, or require realignment and sometimes retuning to move between different q.

We report here on a novel instrument that has been optimized for simultaneous measurement of IXS (especially XRS) at multiple q, for low background from stray scattering, for future measurement of materials in diamond anvil high pressure cells, and for ease and diversity of use by the general users of the light source. Our apparatus uses ten spherically bent Si analyzers, each of which is matched with an independent detector. The analyzers collect scattered radiation over a wide range of q, thus providing ten simultaneous but independent measurements of q-dependent IXS spanning from the low-q, dipole limit to near backscattering from the sample, the maximum allowed momentum transfer. The instrument can be readily extended to perform 19 simultaneous but independent measurements of q-dependent IXS.

[a)]Author to whom correspondence should be addressed; electronic mail: seidler@phys.washington.edu

The total solid angle of the instrument is 0.66 or 1.2% of 4π sr for the present case of 10 analyzers and the expanded case of 19 analyzers, respectively.

Below, we first provide background information on XRS in Sec. II. This includes a brief theoretical treatment, and a more extended discussion of the relationship between XRS and more traditional core shell spectroscopies such as x-ray absorption fine structure (XAFS) and electron energy loss spectroscopy (EELS). In Sec. III we describe the design of our apparatus. In Sec. IV we present the experimental details. Finally, in Sec. V we present several XRS measurements using our apparatus. These include new results for the q-dependent XRS from Mg and also measurement of the XRS from the C K-edge in diamond for means of instrument standardization. We then conclude.

II. BACKGROUND

In an IXS experiment, the energy loss and momentum transfer from the scattering photon to the system are given by

$$\hbar\omega \equiv \hbar\omega_1 - \hbar\omega_2 = E_1 - E_2,$$

$$\mathbf{q} \equiv \mathbf{k}_2 - \mathbf{k}_1, \tag{1}$$

where the "1" and "2" indices refer to the incident and scattered photons, respectively. The nonresonant portion of the double-differential scattering cross section $d^2\sigma/d\Omega d\omega$ naturally separates into a Thomson scattering contribution $(d\sigma/d\omega)_{\text{Th}}$ and the dynamic structure factor $S(\mathbf{q},\omega)$, i.e.,

$$\frac{d^2\sigma}{d\Omega d\omega} = \left(\frac{d\sigma}{d\omega}\right)_{\text{Th}} S(\mathbf{q},\omega)$$

$$= r_0^2(\hat{\varepsilon}_2 \cdot \hat{\varepsilon}_1)^2 \frac{\omega_2}{\omega_1} \sum_f |\langle f|e^{i\mathbf{q}\cdot\mathbf{r}}|0\rangle|^2 \delta(E_f - E_0 - \hbar\omega),$$

$$\tag{2}$$

where r_0 is the classical electron radius, $(\hat{\varepsilon}_2 \cdot \hat{\varepsilon}_1)^2$ is the x-ray polarization factor, and 0 and f label the electron's initial and final states, respectively. Equation (2) provides a basis for understanding all nonresonant IXS, including scattering from phonons, plasmons, valence electrons (Compton scatting), and core shell electrons (XRS). Henceforth, we focus on our discussion on XRS.

The dipole limit in XRS is defined by the condition $qa \ll 1$, where a is the average radius of the initial state of the photoelectron, i.e., of the initial core shell wave function. In this regime, the expansion of the e^{iqr} operator in Eq. (2) can be truncated at the $i\mathbf{q}\cdot\mathbf{r}$ term, thus allowing only dipole transitions ($\Delta l = \pm 1$). Consequently,

$$S(\mathbf{q},\omega) \underset{qa \ll 1}{\longrightarrow} \sum_f q^2 |\langle f|\hat{q}\cdot\mathbf{r}|0\rangle|^2 \delta(E_f - E_0 - \hbar\omega), \tag{3}$$

which is clearly proportional to the x-ray absorption coefficient,

$$\mu = \sum_f \frac{4\pi^2 e^2}{m^2 c \omega_1 n} |\langle f|\hat{\varepsilon}\cdot\mathbf{r}|0\rangle|^2 \delta(E_f - E_0 - \hbar\omega_1), \tag{4}$$

but with $\hat{q}$ playing the role of the polarization direction $\hat{\varepsilon}$ in XAFS or related x-ray absorption spectroscopies.[22] EELS is also usually dipole limited. For electron scattering, the Thomson scattering prefactor in Eq. (2) is replaced by $(d\sigma/d\omega)_{e-e} \propto q^{-4}$, which strongly suppresses high q contributions.

In comparing XAFS and XRS, two issues must be addressed: the different applications in the low-q limit and the additional experimental degree of freedom in XRS provided by the momentum transfer. First, as mentioned above, in the low-q limit XRS and XAFS probe the same transition matrix element and have similar directional sensitivities. Recall, however, that we are specifically concerned with electronic transitions starting from shells with relatively low binding energies, typically 50–600 eV; this includes the K edges of second-row elements, L edges of third-row and some fourth-row elements, etc. Consequently, the requirement for XAFS that the incident photon energy be comparable to the binding energy of the relevant electronic shell can be very restrictive. The low-energy incident x-rays result in a measurement which can be predominantly surface sensitive and which generally requires a vacuum environment or other accommodations. In addition, low-energy x-rays are incompatible with the apparatus needed to create some extreme sample environments, such as high pressure chambers for liquids or solids: the x rays cannot penetrate the walls of the chamber, and hence direct XAFS measurements of first-row elements, for example, cannot be performed inside the diamond anvil cells. XRS measurements, on the other hand, can use hard x-rays (typically 5–10 keV) because it is the energy loss which is relevant for $S(q,\omega)$ [see Eqs. (2) and (3)], not the incident or final photon energy. This results in a measurement which is inherently bulk sensitive, and is compatible with a wide range of sample environments.[12,30,34,36,38]

Hence, even in the dipole limit where the two techniques provide analogous information, XRS and soft x-ray XAFS have significantly different applications because of the differences in the incident radiation used. Three recent studies serve to illustrate this point. First, based on molecular dynamics simulations, x-ray absorption near-edge structure (XANES) calculations, and dipole-limit measurements of XRS, a new local structure for liquid water has been proposed.[34] Second, a high-pressure XRS study of graphite revealed a new, ultrahard form of carbon.[30] Third, a high pressure XRS study of hexagonal boron nitride provided a clean signature of the transition to the hexagonal close-packed polymorph, which could previously be best studied only in pressure-quenched samples.[12] In each of these experiments the large penetration length of the incident hard x-rays was put to good use.

Second, while the XRS measurements in the dipole (i.e., low-q) limit are clearly valuable, additional information about previously forbidden final states can be obtained by studying the XRS when qa becomes larger. In this case, the matrix element in Eq. (2) does not simplify to that of Eq. (3), and higher order selection rules become relevant, beginning with the transitions $\Delta l = 0$ and $\Delta l = \pm 2$. For example, the use of q-dependent XRS has shown itself to be especially suitable for spectroscopy of the final state for core excitons or other preedge resonances.[29,33,39] This information is inher-

ently unavailable from direct measurement of XANES on low-Z elements and is difficult (but sometimes possible[40]) to acquire from EELS measurements.

Key topics in the continuing development of q-dependent XRS as a spectroscopy related to, but unique from, XAFS and EELS will be the theoretical treatment of q-dependence throughout the entire accessible range of energy in $S(q,\omega)$ and improved background subtraction or complete modeling of the valence electron contribution to the Compton scattering. Along these lines, the recent work of Soininen et al.[41] shows great promise to extend ab initio theoretical treatment of q-dependent XRS throughout the entire spectrum, from preedge resonances to the extended fine structure. In that paper, excellent agreement is found between the predictions of a real-space, full-multiple scattering Green's function approach and measurements of the direction- and q-dependent XRS from pure Be.[31] Progress on phenomenological subtraction of the valence Compton scattering may be made with the Bayes-Turchin approach which has recently made significant inroads in XAFS analysis.[42–44] It is, however, important to note that this approach would be well superceded by a full ab initio calculation of the valence Compton background, especially to avoid any possible complications from the weak but measurable fine structure which can occur.[45]

In summary, XRS provides an alternative to, and extension of, existing core shell spectroscopies such as XAFS and EELS. In the limit of small momentum transfer, all such techniques probe the same transition matrix element and can be treated with essentially the same theoretical framework. At higher momentum transfers, XRS becomes sensitive to and may be dominated by nondipole transitions, thus giving new information about the local density of excited states.

III. THE MULTIELEMENT IXS SPECTROMETER

In Figs. 1–5 we present the line drawings of the spectrometer and some of its key subsystems. The components are described in detail in the various figure captions, but further comments are in order for completeness. The major components are the support frame [(A) and (E) in Fig. 1; (A) and (C) in Fig. 2], helium-filled scattering enclosure [(K) in Fig. 1], analyzer modules (Fig. 3), detector assembly (Fig. 4), and sample enclosure and positioning assembly (Fig. 5). We now describe these components in turn.

The support frame was machined from 2.5 cm thick Al jig plate. Large apertures cut in the support frame decrease the overall weight of the apparatus without significantly affecting the stiffness of the support. The vertical plate contains 19 equally spaced locations where analyzer modules can be attached with dowel pins to assist with precise, reproducible positioning. The diffractive elements of the analyzers (described below) are positioned 97.5 cm from the sample location. This plate also supports the scattering enclosure and sample placement assembly. Due to the horizontal polarization of the synchrotron radiation, the vertical scattering plane was chosen to maximize the polarization dependence of the Thomson prefactor in Eq. (2). Also, the placement of all analyzer crystals in a common plane is a natural choice for
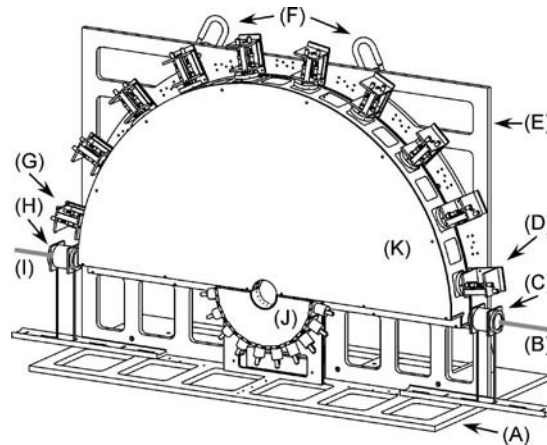

FIG. 1. A line drawing of the multielement XRS spectrometer. *Selected components*: (A) baseplate of the support frame; (B) incident x-ray beam; (C) gas ionization chamber for monitoring the incident intensity; (D) analyzer module for energy loss measurements at high momentum transfer, corresponding to near backscattering from the sample; (E) vertical back plate of the support frame; (F) hoist rings; (G) analyzer module for energy loss measurements at low momentum transfer, corresponding to a relatively small scattering angle from the sample; (H) gas ionization chamber for monitoring the transmitted intensity; (I) transmitted x-ray beam; (J) detector assembly; (K) helium-filled flight path. *Additional description*. For scale, the outer radius of (K) is approximately 95 cm. The sample is located on the rotation axis of the inner, cylindrical region bounded by (J) and (K). Under usual operation, the location of the ten analyzer modules correspond to momentum transfers ranging from 0.8 Å^{-1} (G) to 10.1 Å^{-1} (D) when working at an incident photon energy of ~10 keV.

some applications, such as XRS measurements in diamond anvil cells (DACs) where it is envisioned that a DAC would be placed with a Be gasket in the vertical scattering plane so that all analyzers would be simultaneously illuminated by scattering from the sample in the DAC.

The large distance between sample, analyzer, and detector requires that we use a He-filled flight path. This scattering enclosure [(K) in Fig. 1] was constructed from lucite and polycarbonate plastic and includes Kapton-covered windows for the analyzer faces and for various places where incident, transmitted, or scattered radiation must enter or leave the enclosure. During operation, a small He flow and overpressure are maintained, and the x-ray absorption of the gas in the enclosure is monitored by observing any drifts in the transmission through the entire assembly; this is measured by the final ion chamber [(H) in Fig. 1].

We present line drawings of an analyzer module from two different perspectives in Fig. 3. The spherically bent diffractive elements consist of 250 μm thick float zone Si (111) wafers with 10 cm diameters pressed into and bonded to concave glass lenses having a 1 m radius of curvature (NJXRS-TECH). Each analyzer crystal subtends a solid angle of 8.3×10^{-3} sr from the sample. As can be seen most clearly in Fig. 2, the Rowland circle for each of the analyzer crystals is normal to the vertical scattering plane. The diffractive elements can be rocked through the analyzer's Bragg angle (defining tilts normal to the vertical scattering plane) or normal to it using a kinematic, spring-loaded three-point tilt. By pairing two differential screw micrometers (OptoSigma 133-0201) with stepper motors (MicroMo 1524 containing a 41:1 spur gearhead), we obtained 6 μrad precision and better
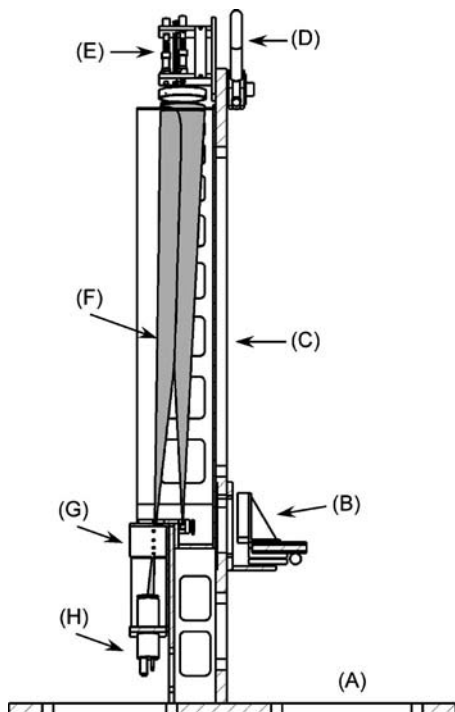
FIG. 2. A section line drawing of the multielement XRS spectrometer, as viewed along the beam direction. *Selected components.* (A) baseplate of the support frame; (B) sample positioning stages; (C) vertical back plate of the support frame; (D) hoist rings; (E) analyzer module for energy loss measurements; (F) ray-tracing cones showing the solid angle of radiation scattered from the sample, then filtered and refocused through a detector aperture (G) and eventually reaching a scintillation detector (H); (G) 5 mm diameter aperture to the detector assembly; (H) scintillation detector. *Additional description.* For clarity of presentation, most of the analyzer modules have been removed in the view and the detector assembly has been sectioned to expose a single scintillation detector.
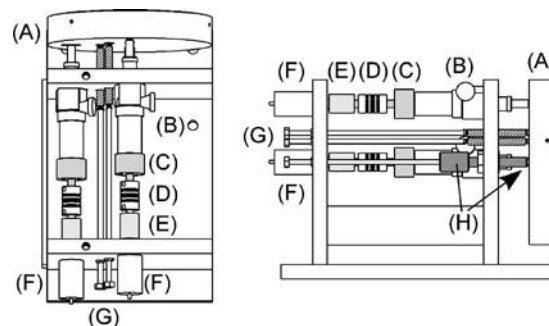

FIG. 3. A line drawing of a tilt-module for a spherically-bent Si analyzer. *Selected components*: (A) holder and spherically bent Si analyzer crystal; (B) differential screw micrometer with nonrotational ball tip; (C) shaft adapter for differential screw micrometer; (D) flexible shaft coupler; (E) shaft adapter for stepper motor; (F) miniature stepper motor with integral gearhead; (G) bolts for applying tension to springs which hold the analyzer holder (A) against the tips of the two micrometers (B) and the central screw (H); the springs are the shaded components at the end of the bolts, connected to the analyzer holder (A); (H) central pivot screw. *Additional description*. For scale, the diameter of the holder of the spherically bent Si analyzer is 11 cm. The back of the analyzer holder (A) has a central depression to seat the ball tip of the central pivot screw, a radial groove for seating the ball tip of first, and a hardened steel flat which is pressed on by the ball tip of the second micrometer.

radiation is scanned. This results in a small dependence on E_1 for the q sampled for each analyzer; this can be ignored when working at small energy losses, but must be included in analysis of data spanning a wide range of energy losses.

In Fig. 4 we show a perspective rendering of the detector assembly with the front cover removed for clarity. The detectors are NaI scintillation detectors with Be windows (Oxford Cyberstar). Strong spatial filtering against stray scattering is provided by 5 mm entrance apertures followed by 16 mm inner-diameter masks placed over the face of the detectors to decrease their exposed size to match the projection of the spherically bent crystal through the entrance apertures.
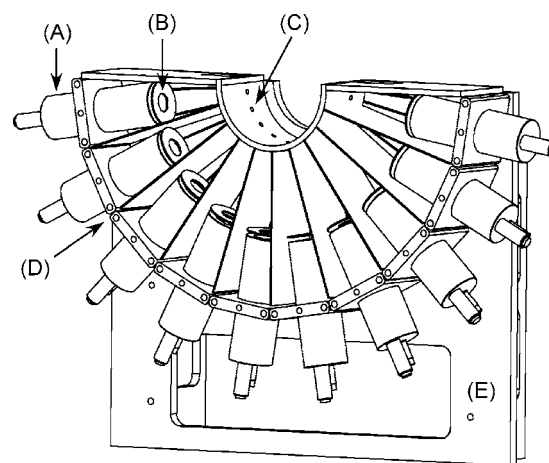
than 50 μrad unidirectional reproducibility, far finer than the width of the rocking curve of the analyzer crystals in typical operating conditions.

The analyzer crystals are prealigned optically by placing a small diode laser (Midwest Laser Products SL650) with a diverging optic at the sample position and then tilting the analyzer crystals so that the laser light is refocused through each corresponding aperture in the detector assembly. Final tuneup references the strong elastic scattering from a polycarbonate sample at the Si (555) reflection at 9890 eV, precisely tuning each analyzer to the same Bragg angle ($2\theta_B = 176.4°$). The stepper motors in the analyzer modules are rapidly driven by a homemade assembly of 20 motor drivers, each based on a stepper motor driver IC (MC3479) and independently controlled by transistor-transistor logic (TTL) pulses from a computer board (Measurement Computing DIO96). This allows rapid, simultaneous alignment of all ten analyzers. After alignment, the motor drivers are turned off. No drift in analyzer tuning was found over many days of subsequent data collection. Under usual operation at the Si (555) reflection with the elastic line at 9890 eV, the scattering angles (from the sample) of the ten analyzers correspond to average momentum transfers of q=0.8, 2.4, 3.9, 5.3, 6.6, 7.7, 8.6, 9.3, 9.8, and 10.1 Å^{-1}, respectively. Data collection proceeds by so-called inverse scanning, where the analyzer crystals are kept fixed and the energy E_1 of the incident

FIG. 4. Line drawing of the detector assembly with the front cover plate removed for clarity of presentation. *Selected components*: (A) scintillation detector; (B) mask for spatial filtering on the face of a scintillation detector; (C) 5 mm aperture in the semicylindrical top of the detector assembly; (D) Al radiation baffle; (E) back support plate for the detector assemble. *Additional description*. The exact location and size of the hole in the mask (B) is chosen so that the cone of radiation collected by the detector [i.e., in the solid angle defined by the hole in the mask and the aperture (C)] matches the cone of radiation focused through the aperture (C) by the appropriate analyzer module.
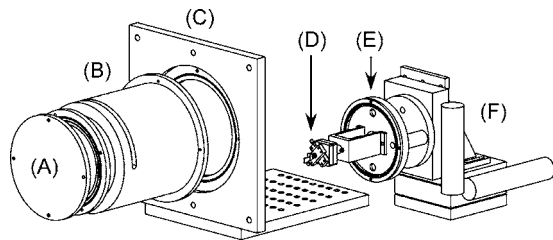
FIG. 5. Line drawing of sample enclosure and positioning assembly with components offset for clarity. *Selected components*: (A) Removable, O-ring-sealed acrylic door; (B) 12.5 cm inner-diameter sample enclosure with 6 mm slot for x rays scattering from sample to analyzer; (C) back support plate for sample enclosure; (D) two-axis manual micropositioning stage (Edmund Optics 38-527) mounted to miniature kinematic stage (Thorlabs KB1X1); (E) support plate for helium connectors, motorized rotation axis (MicroMo 1524A 15/5), and inner flange for flexible membrane; (F) Ball-bearing translation stages (Newport 426A, 433), each driven by an computer-controlled actuator (Zaber T-LA28-S) *Additional description*. A flexible plastic membrane (not shown) seals (C)–(E), providing a closed, He-filled environment while allowing sample positioning in the beam with stages (F).

The vertical slats which separate the detectors eliminate cross talk between detectors due to air scattering within the detector module. A flux of 10^7 counts/s through one aperture induces less than 1 counts/s in the neighboring detector. The entrance apertures to the detector assembly are 102.5 cm from the face of the spherically bent crystals of the analyzer modules, thus defining ten Rowland circles that are perpendicular to the vertical scattering plane, with the sample and the detector entrance apertures offcircle by 2.5 cm. This has negligible effect on energy resolution.[46] When the instrument is later expanded to use 19 analyzers, a modified detector assembly will be analogously designed, i.e, having 19 entrance apertures, baffled segments, and somewhat smaller scintillation detectors.

Finally, in Fig. 5 we show a partly exploded rendering of the sample enclosure and sample positioning assembly. Three-axis positioning is provided by standard translation stages (F) driven by motorized micrometers (Newport 426, 433 linear translation stages; Zaber T-LA28). Sample rotation about the horizontal axis normal to the incident beam is also stepper motor driven. Additional shielding against stray scattering is provided by a 12.5 cm diameter sample enclosure (B) with a slot cut to allow scattering only near the vertical plane. This slot is sealed by a Kapton window and the sample enclosure is sealed to the positioning assembly [i.e., (C) is sealed to (E) in Fig. 5] by a flexible plastic diaphragm. The sample enclosure is then filled with He gas to decrease air scatter and to eliminate ozone formation, a dominant mechanism for beam damage for samples exposed to air. We find that sample exchange and alignment typically take only a few minutes. The relatively large volume of the sample enclosure allows for future modifications for furnaces, cryostats, electrochemical cells, pressure cells, and other extreme sample environments.

IV. EXPERIMENT

All measurements were performed at Sector 20-ID at the Advanced Photon Source x-ray synchrotron. This undulator beam line includes a liquid nitrogen cooled Si (111) double crystal monochromator. The monochromatized radiation is focused by a toroidal mirror to a spot size of 0.3 mm (vertical) by 0.5 mm (horizontal). The incident and transmitted beams were monitored by identical He-filled ionization chambers (Advanced Design Consulting, model 105-1). The incident flux was $\sim 5 \times 10^{12}$ counts/s at 10 keV. All data were collected in inverse scanning mode, where the incident photon energy E_1 is scanned and the analyzer energy kept fixed.

Calibration of the energy loss to within 0.1 eV for each analyzer was obtained by fitting the respective observed profiles for elastic scattering. The full width at half maximum (FWHM) of the elastic scattering for all ten analyzers, and hence the energy resolution, was ~ 1.3 eV in agreement with the theoretical limit for the monochromator. Monochromator drift was small, and was monitored through frequent measurement of the energy for elastic scattering and also by the progressive shift of sharp features in the observed spectra. All data were corrected for variations in incident intensity, for monochromator drift, and for the dependence of the sample absorption and the ion-chamber detector gas absorption on E_1. Finally, $S(q,\omega)$ is then extracted by correcting for the Thomson prefactor in Eq. (2) and employing f-sum rules,[24,37,47] as is standard in this type of IXS measurement. For a sample one penetration length thick in a transmission geometry, we find that the background counting rates were a few to 10 counts/s for each analyzer when at energies where one expects $S(q,\omega) \sim 0$ for the particular sample, i.e., energies well below the elastic line or well past any IXS.

V. RESULTS AND DISCUSSION

In Figs. 6–8 we show $S(q,\omega)$ for a 0.27 mm thick polycrystalline Mg foil (ESPI, 99.9%). The flat face of the foil was normal to the beam, with the beam just below the top edge of the sample. Notice in Fig. 6 the expected progressive shift to higher energy of the Compton scattering with increasing q.[1] In Fig. 7 we show an enlarged view for selected q of the energy loss range where the XRS from the L edges for Mg can be clearly observed. In Figs. 6 and 7, $S(q,\omega)$ for $q = 0.8$ Å^{-1} has been multiplied by 5 for clarity of presentation; all other data have the scale indicated in the figure. The integration time for these data are 28 s/point. For example, for $q = 9.8$ Å^{-1} at an energy loss of 60 eV (i.e., above the $L_{2,3}$ edge at 50 eV), this results in a total of ~ 3400 counts, so that Poisson statistics is negligible on the scale of the figure. Allowing for the different energy resolutions and backgrounds, there is a good agreement between the dipole limit $S(q,\omega)$ observed at the $L_{2,3}$ edge and the classic measurement of soft x-ray absorption in Mg.[48] We will present elsewhere a detailed analysis of these data.[49]

In Fig. 8, we show the XRS from the K edge of Mg. The $1s$ initial state of the K edge has $a \sim 0.07$ Å. Hence, while the data from the highest q will not be strictly dipolar (i.e., it will have $qa \sim 0.7$), it will still be dominated by dipole transitions. By means of example, we integrate the data from all analyzers to provide reasonable statistics for an approximately dipole-limit measurement. The total counting rate is ~ 100 counts/s, and the total measurement time for the data shown is ~ 5 h. The solid line shows the prediction of the
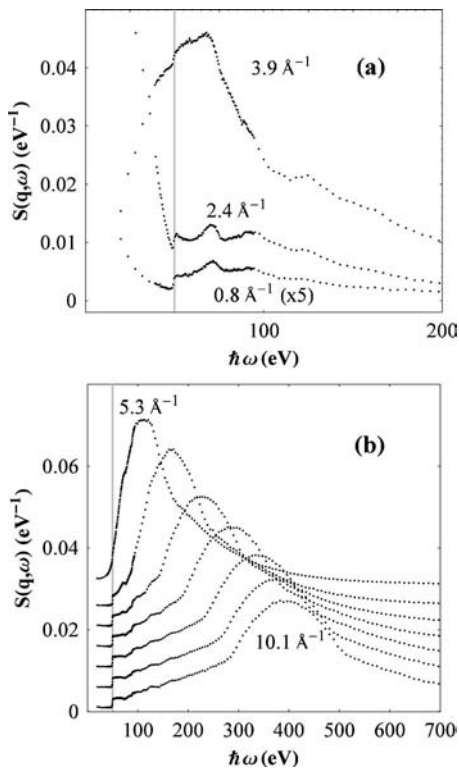
FIG. 6. The dynamic structure function $S(q, \omega)$ for polycrystalline Mg. Data for $q = 0.8$, 2.4, and 3.9 Å^{-1} are shown in the top panel (a), while data for $q = 5.3$, 6.6, 7.7, 8.6, 9.3, 9.8, and 10.1 Å^{-1} are shown in the bottom panel (b). The data in (b) have been shifted vertically for clarity of presentation. Note the expected shift in the Compton profiles as q is increased, in contrast to the fixed $L_{2,3}$-edges at 49.5 eV; the vertical line shows this position.
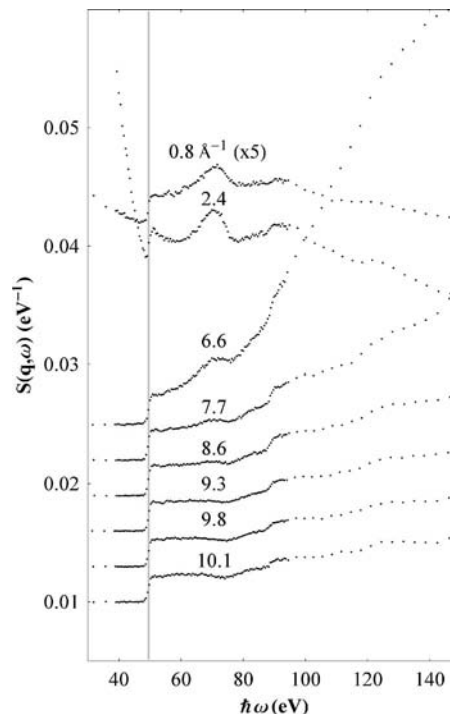

FIG. 7. An enlarged view of $S(q, \omega)$ for Mg for the first 100 eV past the $L_{2,3}$ edge (50 eV) at dipole-limited momentum transfers (0.8 and 2.4 Å^{-1}) and at high-q (6.6–10.1 Å^{-1}). Data have been shifted along the vertical axis for clarity. The 3.9 and 5.3 Å^{-1} spectra were omitted from this graph due to the significant valence Compton background. The vertical line shows the position of the $L_{2,3}$ edge (49.5 eV). Note that the L_1 edge (89 eV) increases in strength at intermediate and higher momentum transfers.

x-ray absorption coefficient by FEFF8.2 (Ref. 50) using a standard path expansion. The agreement between theory and measurement is generally good, and reflects the equivalence of XRS and XAS in the dipole limit [Eqs. (3) and (4)]. The disagreement between theory and experiment is primarily within the first 10 eV of the edge where FEFF is most sensitive to the photoelectron's self-energy and the effect of the core hole.

For means of standardization to allow comparison with other apparatus, in Fig. 9 we present the XRS measurements at a momentum transfer of 3.9 Å^{-1} for the C K-edge of a synthetic diamond sample. The sample was a rectangular parallelepiped with a thickness of 2.0 mm in the beam direction; the beam was positioned just below the top face of the sample. The data have been normalized for fluctuations in the overall intensity of the incident beam. The XRS intensity at the edge is $\sim 6 \times 10^3$ counts/s on a valence Compton contribution of a few hundred counts/s. The XRS intensity and the valence Compton contribution to the IXS are both strong functions of q, so that integrating the same energy loss region across all ten analyzers results in 5.7×10^4 counts/s in the C K-edge XRS above a valence Compton signal of 1.1×10^5 counts/s.

Before concluding, we briefly discuss the potential for DAC measurements in our instrument. While the overall geometry of the instrument is ideally suited for DAC measurements with the gasket in the vertical scattering plane (i.e., the load axis in the horizontal plane and perpendicular to the incident beam), two issues will need to be addressed before

high-throughput XRS measurements in DACs are viable. First, it will be important to have a narrower focus for the incident beam, down to perhaps 20 μm in the horizontal when working at very high pressures, so that all of the incident intensity will penetrate between the diamonds. Second, it will be important to add spatial filtering at the DAC to minimize the contribution to the overall IXS signal from the DAC gasket.

In conclusion, we have constructed a multielement spectrometer that simultaneously measures the nonresonant inelastic x-ray scattering (IXS) at ten different momentum transfers q with ~ 1 eV resolution. This instrument has been optimized for low background counts, for ease of use, for future use with diamond anvil cells, and for straightforward expansion to perform simultaneous measurements of IXS at
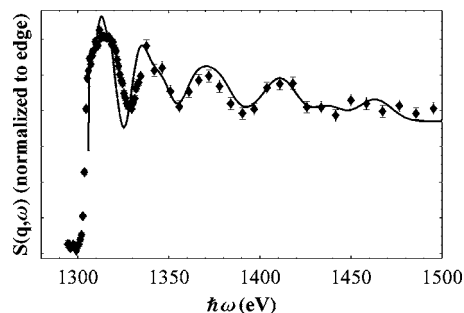

FIG. 8. The measured, dipole limit $S(q, \omega)$ for polycrystalline Mg in the range of the Mg K-edge (1305 eV). The solid line is the x-ray absorption coefficient calculated by FEFF8.2 (Ref. 49). A constant factor was used to put the measurement and theory on the same scale.
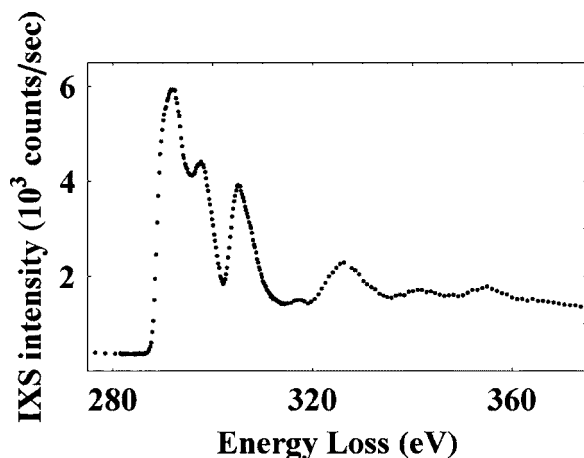
FIG. 9. The measured intensity of the inelastic x-ray scattering from diamond at $q=3.9$ Å^{-1}. There is a total measurement time of 10 s/point. The errors from Poisson statistics are the size of the symbols or smaller.

19 different q. Our new results on the IXS from the L and K edges of Mg illustrate the most direct capabilities of the new spectrometer. This instrument is now available to general users of the Advanced Photon Source as the lower energy resolution inelastic x-ray (LERIX) scattering spectrometer; it serves to complete the nonresonant IXS capabilities at this facility by complementing the planned capabilities of the high energy resolution (HERIX, resolution ~1 meV) and medium energy resolution (MERIX, resolution ~100 meV) spectrometers which are now under construction.[51]

ACKNOWLEDGMENTS

[1] W. Schulke, *Handbook on Synchrotron Radiation*, edited by G. Brown and D. E. Moncton (Elsevier, Amsterdam, 1991), Vol. 3, Chap. 15.

[2] *X-ray Compton Scattering*, edited by M. J. Cooper (Oxford, New York, 2004).

[3] A. H. Compton, *X-rays as a Branch of Optics* (Elsevier, New York, 1965).

[4] U. Bergmann, P. Glatzel and S. P. Cramer, Microchem. J. **71**, 221 (2002).

[5] W. Schulke, J. Phys.: Condens. Matter **13**, 7557 (2001).

[6] P. A. Montano and A. T. Macrander, J. Phys. Chem. Solids **61**, 415 (2000).

[7] S. Mainninen, J. Phys. Chem. Solids **61**, 335 (2000).

[8] E. E. Alp, W. Sturhahn, T. S. Toellner, J. Zhao, M. Hu, and D. E. Brown, Hyperfine Interact. **144**, 3 (2002).

[9] E. Burkel, Rep. Prog. Phys. **63**, 171 (2000).

[10] W. Schulke and H. Nagasawa, Nucl. Instrum. Methods Phys. Res. A **222**, 203 (1984).

[11] M. Shwoerer-Boerning, A. T. Macrander, P. M. Abbamonte, and D. A. Arms, Rev. Sci. Instrum. **69**, 3109 (1998).

[12] Y. Meng *et al.*, Nat. Mater. **3**, 111 (2004).

[13] G. Monaco, A. Cunsolo, G. Ruocco, and F. Sette, Phys. Rev. E **60**, 5505 (1999).

[14] C. C. Kao, K. Hamalainen, M. Krisch, D. P. Siddons, T. Oversluizen, and J. B. Hastings, Rev. Sci. Instrum. **66**, 1699 (1995).

[15] T. Suzuki, J. Phys. Soc. Jpn. **22**, 1139 (1967).

[16] H. Nagasawa, J. Phys. (Paris) **48**(C-9), 863 (1987).

[17] K. Tohji and Y. Udagawa, Phys. Rev. B **36**, 9410 (1987).

[18] W. Schülke, A. Berthold, A. Kaprolat, and H.-J.. Güntherodt, Phys. Rev. Lett. **60**, 2217 (1988).

[19] T. Suzuki, A. Tanokura, and N. Arimitsu, J. Phys.: Condens. Matter **1**, 5187 (1989).

[20] K. Tohji and Y. Udagawa, Phys. Rev. B **39**, 7590 (1989).

[21] K. Tohji, Y. Udagawa, T. Matsushita, M. Nomura, and T. Ishikawa, J. Chem. Phys. **92**, 3233 (1990).

[22] N. Watanabe, H. Hayashi, Y. Udagawa, K. Takeshita, and H. Kawata, Appl. Phys. Lett. **69**, 1370 (1996).

[23] M. H. Krisch, F. Sette, C. Masciovecchio, and R. Verbeni, Phys. Rev. Lett. **78**, 2843 (1997).

[24] H. Nagasawa, S. Mourikis, and W. Schulke, J. Phys. Soc. Jpn. **66**, 3139 (1997).

[25] Y. Udagawa, N. Watanabe, and H. Hayashi, J. Phys. IV **7**, 347 (1997).

[26] D. T. Bowron, M. H. Krisch, A. C. Barnes, J. L. Finney, A. Kaprolat, and M. Lorenzen, Phys. Rev. B **62**, R9223 (2000).

[27] W. A. Caliebe, J. A. Soininen, E. L. Shirley, C.-C. Kao, and K. Hämäläinen, Phys. Rev. Lett. **84**, 3907 (2000).

[28] U. Bergmann, P. Wernet, P. Glatzel, M. Cavalleri, L. G. M. Pettersson, A. Nilsson, and S. P. Cramer, Phys. Rev. B **66**, 092107 (2002).

[29] K. Hämäläinen, S. Galambosi, J. A. Soininen, E. L. Shirley, J.-P. Rueff, and A. Shukla, Phys. Rev. B **65**, 155111 (2002).

[30] W. Mao *et al.*, Science **302**, 425 (2003).

[31] C. Sternemann *et al.*, Phys. Rev. B **68**, 035111 (2003).

[32] U. Bergmann, H. Groenzin, O. C. Mullins, P. Glatzel, J. Fetzer, and S. P. Cramer, Pet. Sci. Technol. **22**, 863 (2004).

[33] Y. Feng, G. T. Seidler, J. O. Cross, A. T. Macrander, and J. J. Rehr, Phys. Rev. B **69**, 125402 (2004).

[34] P. Wernet *et al.*, Science **304**, 995 (2004).

[35] D. A. Arms, T. J. Graber, A. T. Macrander, R. O. Simmons, M. Schwoerer-Böhning, and Y. Zhong, Phys. Rev. B **71**, 233107 (2005).

[36] S. K. Lee, P. J. Eng, H. K. Mao, Y. Meng, M. Newville, M. Y. Hu, and J. F. Shu, Nat. Mater. **4**, 851 (2005).

[37] C. Sternemann, J. A. Soininen, S. Huotari, G. Vankó, M. Volmer, R. A. Secco, J. S. Tse, and M. Tolan, Phys. Rev. B **72**, 035104 (2005).

[38] P. Wernet, D. Testemale, J. L. Hazemann, R. Argoud, P. Glatzel, L. G. M. Pettersson, and A. Nilsson, U. Bergmann, J. Chem. Phys. **123**, 154503 (2005).

[39] Y. Feng, Ph.D. dissertation, University of Washington, 2003.

[40] See, for example, J. J. Ritsko, S. E. Schnatterly, and P. C. Gibbons, Phys. Rev. B **10**, 5017 (1974).

[41] J. A. Soininen, A. L. Ankudinov, and J. J. Rehr, Phys. Rev. B **72**, 045136 (2005).

[42] K. V. Klementev, J. Phys. D **34**, 209 (2001).

[43] H. Rossner and H. Krappe, J. Synchrotron Radiat. **8**, 261 (2001).

[44] J. J. Rehr, J. Kozdon, and J. Kas, J. Synchrotron Radiat. **12**, 70 (2005).

[45] M. Hakala, S. Huotari, K. Hämäläinen, S. Manninen, Ph. Wernet, A. Nilsson, and L. G. M. Pettersson, Phys. Rev. B **70**, 125413 (2004).

[46] P. Suortti, P. Pattison, and W. Weyrich, J. Appl. Crystallogr. **19**, 336 (1986); **19**, 343 (1986); **19**, 353 (1986).

[47] P. Eisenberger and P. M. Platzman, Phys. Rev. A **2**, 415 (1970).

[48] H.-J. Hagemann, W. Gudat, and C. Kunz, DESY Report No. 74/7, 1974.

[49] T. T. Fister, G. T. Seidler, C. Hammer, J. O. Cross, J. J. Rehr, and J. A. Soininen (unpublished).

[50] A. L. Ankudinov, B. Ravel, J. J. Rehr, and S. D. Conradson, Phys. Rev. B **58**, 7565 (1998).

[51] E. Alp *et al.*, Synchrotron Radiat. News, **19**, 31 (2006).